DOI: 10.1784/insi.2022.64.6.XXX

Efficient algebraic image reconstruction technique for computed tomography

R Hanna, M Sutcliffe, P Charlton and S Mosey

Industrial computed tomography (CT) has seen widespread adoption within certain areas of non-destructive testing (NDT), with many commercial systems capable of acquisition and reconstruction of cone-beam CT data. The majority of these systems utilise reconstruction algorithms based on the traditional filtered back-projection (FBP) methods, which are imperfect with respect to limited-angle cone-beam data. These techniques are also inherently restricted in the source trajectories that can be utilised due to the use of Fourier slice theorem. This restricts FBP-based techniques to a circular or helical trajectory. Iterative reconstruction algorithms provide a solution to these limitations as the volume reconstruction does not depend on the location or orientation of the source and detector, allowing the possibility of scanning trajectories that satisfy well-known CT data-sufficiency conditions. This paper proposes a method of reconstruction based on computationally efficient computer graphics algorithms data collected from points in 3D space not restricted to a single circular trajectory, which is useful within NDT for automated robotic inspection. The algorithms developed allow for rapid processing of the algebraic reconstruction technique (ART) for use with X-ray transmission data for CT reconstruction. Experimental results are presented for reconstructions for circular trajectory and points on a sphere to demonstrate the suitability for NDT applications.

1. Introduction

Since the innovation of cone-beam X-ray projections for computed tomography (CT), volume reconstruction has typically been achieved using filtered back-projection (FBP) methods, which are founded on Fourier slice theorem[1]. Initially developed for parallel-beam projection, the technology has been adapted for use with fan-beam projection and later cone beam. The most widely used 3D reconstruction algorithm for CT is the Feldkamp, Davis and Kress (FDK) algorithm[1], which uses the 3D cone-beam model at speeds much faster than the fan-beam data acquisition methods. However, in order to achieve this, some transformations are required to approximate a parallel-beam acquisition due to limitations within the FDK reconstruction algorithm[2]. This process is referred to as cone-beam re-binning. The FDK algorithm therefore produces an approximation method to cone-beam image reconstruction but is computationally efficient and practical where sufficient rotational information is available.

In contrast, iterative reconstruction methods for X-ray imaging have been around for many years[3]. While they offer an accurate (rather than approximate) solution for volume reconstruction, it comes at the cost of computational time. Initially developed in the 1970s, the algebraic reconstruction technique (ART) (described later in Section 2) was introduced at a time when contemporary computing power was limited. The ART algorithm has no computational dependencies between individual ray-sums or projections, making modern parallel computing processing techniques applicable to aid in the reduction of volume reconstruction speed. While parallel processing systems have existed for many years (for example the Cray-1 supercomputer of the 1970s), it was not until the 2010s that computing power for parallel processing became affordable for consumer use. Technological advancements such as compute unified device architecture (CUDA) allow for general-purpose computing to be performed on specialised hardware, such as a graphics processing unit (GPU)[4]. This allows for high levels of parallelisation to occur during code execution, utilising a brute-force approach to achieve computational speed as seen in non-destructive testing (NDT) applications[5].

As NDT inspection components increase in geometrical complexity and size, the ability to inspect with CT systems becomes more challenging, in part due to limited access and restricted scanning trajectories. The ability to locate the part inside a traditional CT cabinet in an orientation that will allow sufficient quality of data to be obtained is critical to the ability to provide a reconstruction that can be useful for accurate measurements of dimensions or defects. This problem is noticeable in components with a high height-to-width ratio (HWR), such as planar samples[6]. If the acquisition strategy used is a circle of source and detector points limited to a single plane aligned with the reconstruction grid axes, as described in[1] and referred to from here on as a circular trajectory, this can cause limitations on the angular range allowable to ensure sufficient X-ray penetration. This problem has previously been researched through the use of iterative algorithms such as ART[3] and the simultaneous algebraic reconstruction technique (SART)[7], due to their ability to provide improved reconstructions with less data than that of the FDK algorithm.

An alternative to placing restrictions on the range of data that can be acquired in a circular trajectory is to increase the degrees of freedom of the source and detector. The use of a circular trajectory with a cone-beam geometry, as in the FDK algorithm (due to the

Submitted 06.01.22 / Accepted 04.05.22

Ross Hanna is with the Wales Institute of Science and Art (WISA), University of Wales Trinity Saint David.

Dr Mark Sutcliffe is with VAL, TWI.

Professor Peter Charlton is with the School of Engineering, Manufacturing & Logistics, University of Wales Trinity Saint David.

Dr Stephen Mosey is with the School of Applied Computing, University of Wales Trinity Saint David.

use of the Fourier slice theorem), does not fulfil the requirements for a mathematically exact reconstruction, as shown by Tuy[8] and Smith[9]. As iterative image reconstruction methods use a ray-tracing-based model to obtain the voxels that contribute to the measured attenuation, there is no limitation on the trajectory or position of the X-ray source and detector. This flexibility allows the source to traverse points on a sphere or indeed any arbitrary geometry (such as a robotic path), increasing the number of views to be obtained of a region.

The ability to perform arbitrary scanning of an object without the requirement for a cabinet system would be of great benefit to NDT, where larger components require inspection. This added flexibility allows scanning of components that were previously infeasible but now possible using new technologies such as robotic systems. This paper explores methods for volume reconstruction at computationally efficient speeds with source and detector positions not restricted to a single circular trajectory, to create a practical NDT solution with applications to robotic systems.

2. Theoretical background

The algebraic reconstruction technique was proposed by Gordon *et al*[3] for 3D electron microscopy and X-ray photography. It has since been widely researched for use in X-ray computed tomography (XCT) as an alternative to analytical techniques such as the FDK algorithm. The basic principle is to find which voxels are intersected by the X-ray and to provide a weighted contribution based on the pixel detector value and voxel intersection properties. The geometric configuration, as used in this paper, is shown in Figure 1. The ART algorithm considers a 3D grid (V) of voxels that contain the calculated attenuation coefficients of the object. These coefficients are calculated through summation along a ray path from the source to the ith detector pixel, where the intersection path throughout the voxel volume can be used to calculate the weighting coefficient W_{ij}, a correction factor based on the contribution of each voxel to the ray sum. W_{in} is the total length of the ray within the voxel volume.

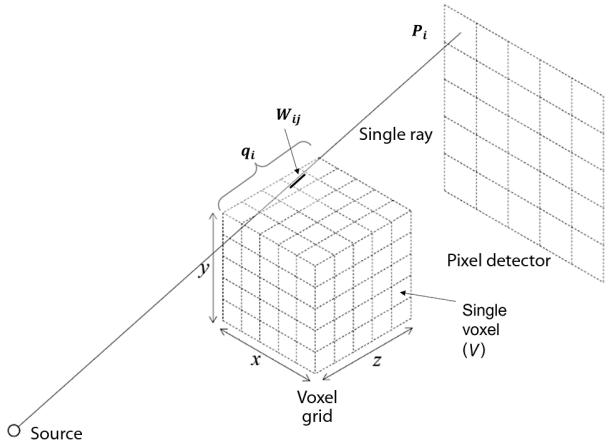

Figure 1. Illustration of the coordinate system used in this work

The ART algorithm as expressed in equation form for voxel volume reconstruction is as follows:

$$V_j^{(k+1)} = V_j^{(k)} + \lambda \frac{(P_i - q_i)}{\sum_{n=1}^{N} W_{in}^2} W_{ij} \quad \ldots\ldots (1)$$

where q_i is the sum of the forward-projection operation for the ith ray based on the current grid values determined by k iterations, j is the voxel index, i is the row index value (pixel index in XCT) and n is the voxel index for the ith ray. The value of the forward projection, q_i, is calculated as:

$$q_i = \sum_{n=1}^{N} W_{ij} V_n^{(k)} \quad \ldots\ldots (2)$$

where P_i is the measured value from the input images and the difference between the measured value P_i and the calculated ray sum q_i is applied to the relevant voxels based on the calculated weight and the relaxation factor λ.

The ART algorithm uses a weighted contribution (the W term) to represent the sum along a ray path through the 3D voxel grid. The simplest of the techniques to determine the weight uses a binary method; if a voxel has been intersected by the ray, the corresponding weighting contribution is given a value of 1. The weighting contribution can be formulated as coefficients of a system of linear equations, with the coefficients for each element of the voxel grid calculated as the product of the weight of the voxels W_{ij} and the attenuation coefficient $V_n^{(k)}$ for each projection position.

A method to improve the weighted contribution is to use the line integral method (LIM)[10], where the normalised length of the ray within a voxel is used as the coefficient, which improves the accuracy of the contribution of the voxels to the attenuation coefficient of the pixels. Considering the binary weighting method and Figure 2, if a voxel is intersected by either path A or path B, then the weight values assigned would be 1 regardless of the ray intersection length. In the case of the LIM, however, path A is given a weighted value of 1 (as it traverses the longest possible path through the voxel), but ray B is given a weighted contribution of 0.25 (which is proportional to the maximum possible).

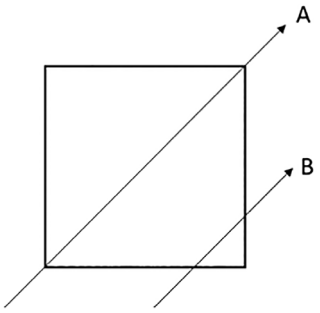

Figure 2. Line integral model

Two immediate computational problems present themselves with respect to the ART equation: firstly, how to algorithmically determine which voxels are intersected by a given X-ray; and secondly, how to compute the LIM weighted value. These will be explored in the next section.

2.1 Efficient ray-voxel intersection

As previously discussed, the set of intersected voxels in 3D space for a given ray results in only a small number of voxels with respect to the entire volume. Defining the voxel intersection problem in the context of 2D computer graphics is conceptually identical to standard line drawing methods, where the algorithm aims to define which pixels in 2D space to illuminate. This is a well-defined problem, with the most common method being to use a variation of the digital differential analyser (DDA) algorithm[11]. Originally developed for 2D graphics, Amanatides and Woo[12] extended this concept to 3D voxel traversal. In their work, the DDA algorithm was adapted to 3D and extended to have no preferred axis, making it both computationally efficient while prohibiting more than one axis change per traversal step. For a ray in parametrised form, as shown in Equation (3), the value of t for the three axes x, y and z

is calculated, where the minimum of the three values indicates the distance along the ray that is within the current voxel:

$$\vec{r} = \overrightarrow{r_0} + t\vec{v} \quad \text{..... (3)}$$

To support this, it is preferable to define the coordinate space as a series of axis-aligned bounding boxes (AABB) representing the voxels, where if a voxel is traversed, the coordinates are assigned to ObjectList[X][Y][Z], which represents the 3D grid of voxels. A definition of this algorithm is given in the pseudocode below:

Pseudocode 1: Voxel traversal algorithm

```
list= NIL;
do      {
        if(tMaxX < tMaxY) {
                if(tMaxX < tMaxZ) {
                        X= X + stepX;
                        if(X == justOutX)
                                return(NIL); /* outside grid */
                        tMaxX= tMaxX + tDeltaX;
                } else  {
                        Z= Z + stepZ;
                        if(Z == justOutZ)
                                return(NIL);
                        tMaxZ= tMaxZ + tDeltaZ;
                }
        } else  {
                if(tMaxY < tMaxZ) {
                        Y= Y + stepY;
                        if(Y == justOutY)
                                return(NIL);
                        tMaxY= tMaxY + tDeltaY;
                } else {
                        Z= Z + stepZ;
                        if(Z == justOutZ)
                                return(NIL);
                        tMaxZ= tMaxZ + tDeltaZ;
                }
        }
        list= ObjectList[X][Y][Z];
} while(list == NIL);
return(list);
```

The calculation of the LIM weight may then be obtained by extending the slab algorithm[13] to 3D space. The slab method is a computationally efficient method for determining the length of the intersecting line through a 2D box (as illustrated in Figure 3) and extending it to 3D space for this work is trivial.

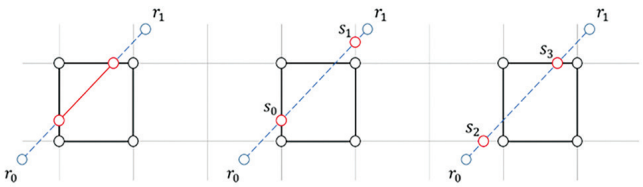

Figure 3. Bounding box coordinate nomenclature

A slab is defined as a bounding volume between two parallel planes with a finite distance separating them, expressed as a normal vector to one of the planes. The bounding volume intersection is first calculated as the ray intersection, from r_0 to r_1, for each slab, represented by S_0 and S_1 for the y-axis and S_2 and S_3 for the x-axis, which are then used to calculate the intersection of the intervals. The intersection of the intervals is calculated as the maximum of the near values and the minimum of the far values.

3. Implementation of algorithms

Circular trajectories use a fixed source and detector and a rotating platform to obtain a series of projections at equal angular spacing. This acquisition strategy is the simplest to physically implement using a rotating platform, although the accuracy of reconstructed planes decreases when further away from the plane of the source and detector due to the divergence of the cone beam when using reconstruction algorithms such as FDK. Algebraic reconstruction methods are not inherently restricted in the geometries or trajectories used, so long as the positions and orientations of the source, detector and volume can be accurately represented. This allows greater flexibility in the positions and orientations, which can be used to obtain projections to improve the reconstruction quality. The circular trajectory for a 2D voxel grid fully satisfies the necessary data sufficiency conditions; however, these are no longer satisfied when cone-beam acquisition geometry is used, as all of the object intersection planes do not intersect the source trajectory at least once as in the Tuy-Smith condition[8,9]. The simplest analogue of the circular trajectory in 2D space is a spherical trajectory in 3D space. The use of a spherical trajectory has the added benefits of multiple views from orthogonal positions, allowing in two or three projections to determine the approximate position of a defect in the x, y and z coordinates.

The source and detector locations for an arbitrary trajectory are defined by positions in 3D space using the cartesian coordinates x, y, z. The orientation of both the source and detector are defined using an axis-angle representation, to allow the position and orientation of the source and detector to be characterised individually. This is required when the source orientation is not normal to the surface of the detector, either due to positional errors, which is more important in robotic acquisition, or intentional, to allow for alternative scanning strategies such as laminographic scanning. This is where the detector and source are kept stationary and the component is moved with linear motion between the source and detector.

The spherical trajectory with locations of the source and detector placed on the surface of a sphere with equiangular spacing determined by a single parameter $\Delta\theta$, which denotes the angular spacing between all points, has a large amount of data redundancy, allowing a reduction in the number of projections. The number of projections on a circular path can be determined using Equation (3) to be approximately 480 projections for a full rotation with an angular spacing $\Delta\theta$ of 0.75°:

$$N_p = \frac{\pi N_x}{2} \quad \text{..... (4)}$$

where N_x is the number of voxels in the x and y axes. For the volume of a side length of 300 voxels (as used in the later experimental configurations), the minimum number of projections N_p is 472 over a range of 0° to 360°.

Using the same spacing for an equiangular spherical trajectory to allow direct comparison, where a full 360° rotation with a 0.75° angular spacing, followed by a tilt of 0.75° over 180° until the sphere is fully sampled would yield 115,200 projections (480 × 240 projections), as shown in Figure 4, a value much larger than necessary for a fully determined system of linear equations.

There has been a significant amount of interest in the use of ART-based algorithms for reconstruction of CT data acquired using non-traditional scanning modalities[14,15]. For the circular trajectory, the source moves in the XZ plane of the coordinate system of the reconstruction volume.

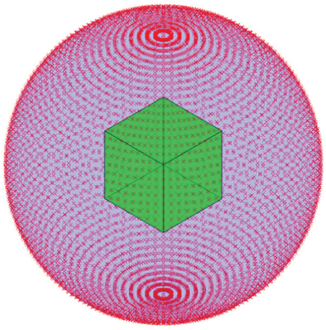

Figure 4. Illustration of the spherical trajectory

This is implemented within floating-point memory on the GPU as two voxel datasets; the current iteration answer and the weight correction coefficients. For a single source position and the corresponding projection, a ray path from the source to each detector pixel is created and passed to a GPU for processing, as illustrated in Figure 5.

Each CUDA processing thread calculates the voxels intersected by the ray path dynamically using the ray-voxel intersection algorithm, as described in Section 2.1. A corresponding line weight is then calculated. Each thread calculates the contribution of the individual detector pixels to the volume using the ART equation and the calculated values are applied to the relevant voxels. A pre-calculation step is performed for each ray path to check that it intersects the reconstruction volume. This is performed using the slab method, with the volume being represented by a single voxel and the number of voxels in each dimension as the size. If the ray path for a given detector pixel does not intersect the volume, the processing for the ray path is terminated. The implementation of the algorithm means that each projection can be calculated with no dependence on any other projection. This lack of dependence and the algorithms used for the ray traversal calculations allows the non-circular reconstruction to be performed with no additional computational cost compared to the circular reconstruction.

When using a single ray path per detector pixel, located at its centre, the issue of over-sampling (and under-sampling) may become problematic. The limitation of a single ray path per detector pixel presents itself as voxels with a high attenuation coefficient that is disproportionate to the surrounding voxels, due to a single voxel being sampled many times within a single projection and other voxels being under-sampled or missed due to the divergent nature of the beam. This effect is illustrated in Figure 6, where the pixel values of 0.9, 0.7 and 0.8 are back-projected. This leads to a voxel that is sampled by all three pixels, with the result being the sum of the three pixel values, shown in Figure 6(b) as the bottom middle voxel with a value of 2.4. By subsampling the detector pixel and keeping track of the number of times a voxel has been intersected, a correction can be applied by dividing the voxel value by the number of intersections to give an average voxel attenuation coefficient.

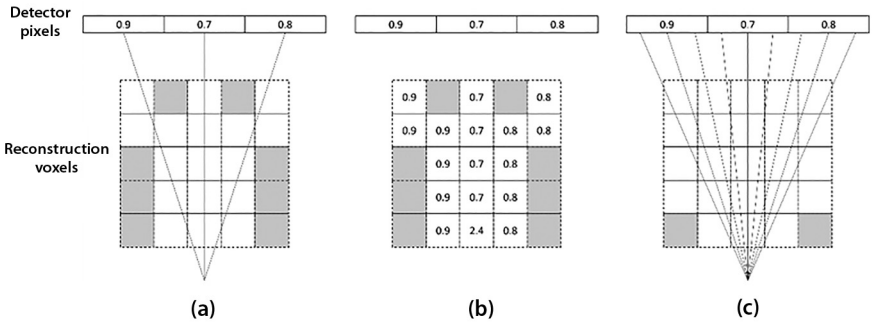

Figure 6. Artefact suppression: (a) original; (b) back-projection; and (c) subsampling

4. Experimental configuration

To evaluate and compare the quality of the reconstructions for the circular and spherical trajectories, the acquisition and reconstruction were simulated for scenarios with full access and limited access. The simulated projections are modelled as noiseless and with a point X-ray source, to allow investigation of the reconstruction algorithms in an ideal set-up. For the circular trajectory, this is equivalent to a full 360° acquisition and a 120° limited-angle acquisition. The object being reconstructed was the Shepp-Logan[16] phantom, with a side length of 300 voxels. This was chosen due to its use as a common point of reference within the literature[17]. The projections were simulated by forward-projecting through the volume to create a 400 × 400 detector pixel projection at a 16-bit data resolution. The geometry used within the system consisted of a source-to-object distance of 573.8 mm, a source-to-detector distance of 1147.8 mm and a detector pixel pitch of 0.2 mm. This is consistent with a typical cabinet system, such as the Nikon XT H 225 CT unit.

These projections were reconstructed using 50 iterations of the ART algorithm to achieve a convergence criterion of 5×10^{-5} between iterations. This convergence behaviour is shown in Figure 7. The reconstructions were performed on a 64-bit Windows 10 Professional PC using an Intel i9-9900KF CPU running at 3.60 GHz as a host for the Nvidia RTX-3090 GPU.

In total, six experimental configurations were explored, consisting of a range of circular and spherical data acquisition strategies over a range of limited and full angular coverage. These are illustrated in Figure 8 and Table 1.

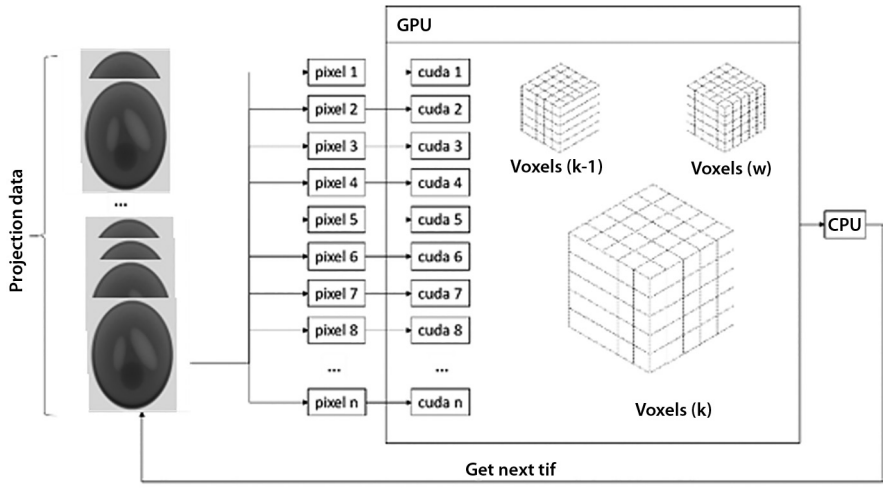

Figure 5. Data partitioning for parallel processing algorithms

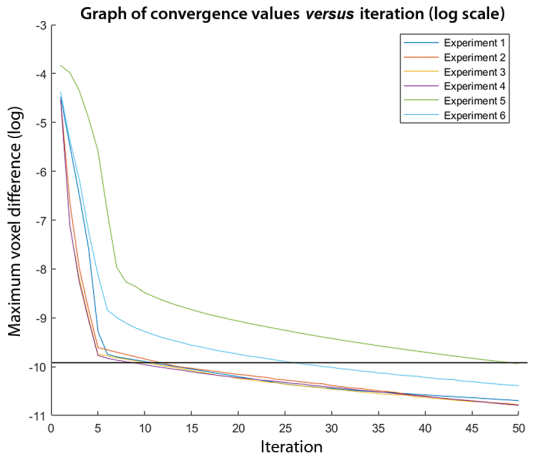

Figure 7. Convergence of the six experimental configurations

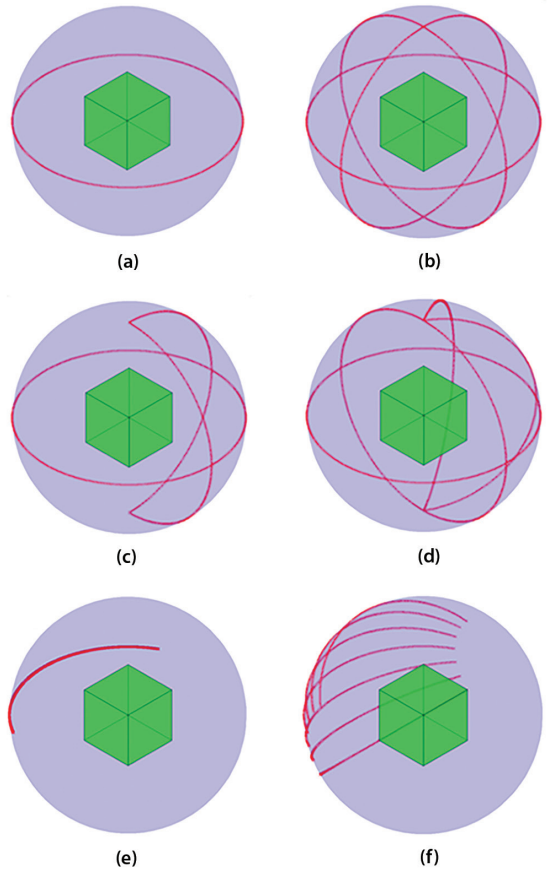

Figure 8. Experimental configurations for: (a) circular full scan; (b) spherical orthogonal full scan; (c) spherical limited orthogonal full scan; (d) spherical multi-path full scan; (e) circular limited-angle; and (f) spherical limited-angle

To provide a baseline comparison against commercial cabinet systems, an initial experimental configuration was established that used the full 360° rotation with an angular increment of 0.25°. A series of noiseless projections were simulated using the forward-projection model and then reconstructed using the ART algorithm. This method is repeated for all further experiments. This configuration is illustrated in Figure 8(a) and is referred to in Table 1 as Experiment 1.

To evaluate the use of a spherical trajectory, a configuration is presented with a source and detector rotation around the *x*, *y* and *z* axes. The use of the *x*, *y* and *z* axis rotation is chosen to allow for the object to be imaged for each plane along an axis. This contrasts with the circular trajectory, where the rotation plane is never imaged directly. The angular increment between projections for a rotation around a single axis is 0.75°. The angular increment has been chosen to allow for comparison between circular and spherical configurations with an equal number of projections. This configuration is illustrated in Figure 8(b) and is referred to in Table 1 as Experiment 2.

To verify the robustness of the proposed strategy, the angular range of the source and detector were restricted to 180° for the *x* and *z* axes. This reduces the total number of projections from 1440 to 960 with a minimal loss of accuracy, as shown by Wang *et al*[18]. This scanning strategy reduces the reconstruction time and, for a physical system, the acquisition time would be reduced. This configuration is illustrated in Figure 8(c) and is referred to in Table 1 as Experiment 3.

To further assess the effect of non-circular source and detector positions, Experiment 4, as illustrated in Figure 8(d), demonstrates acquisition from locations distributed on the surface of a sphere with no dependence on the use of a Cartesian axis.

Inspection in NDT applications can frequently be limited by the component size or geometry. These factors reduce the access available to the component, reducing the available angles that projections can be obtained from. For two-dimensional fan-beam geometry, the minimum angle required for a mathematically exact reconstruction to be possible is 180° plus the fan angle, known as the half scan[18]. The use of an angular range less than the half scan results in an ill-posed process[19] and is known to cause artefacts in the reconstruction[20].

To investigate the performance of the spherical reconstruction method in the limited-angle case, a circular trajectory was first used with a rotation from 30° to 150° as a baseline. The resultant angular range of 120° (Experiment 5), as shown in Figure 8(e), is a limited-angle acquisition that would be necessary in a cabinet system where larger angular ranges are not possible due to the component size or geometry.

The trajectory for Experiment 5 was extended to a non-circular trajectory to demonstrate limited-angle acquisition. The trajectory occupies an angular range from −45° to 45° in a

Table 1. Description of all experimental configurations

Experiment	Figure	Trajectory	Angular range (*y*-axis)	Angular range (*x*, *y*, *z*)			Projections
1	8(a)	Circular	360	–	360	–	1440
2	8(b)	Spherical	360	360	360	360	1440
3	8(c)	Spherical	360	180	360	180	960
4	8(d)	Spherical	360	360	360	180	1440
5	8(e)	Circular	30-150	–	120	–	1120
6	8(f)	Spherical	30-150	90	120	–	1120

direction orthogonal to the primary scanning direction of Experiment 5. This is referred to as Experiment 6 and is illustrated in Figure 8(f). The angular increment used was 0.75°, resulting in a total of 1120 projections. This number of projections was also used in Experiment 5 to ensure consistency between the two limited-angle experiments.

5. Results and discussion

All data was normalised between 0 and 1 using min-max normalisation (Equation (4)) to allow direct comparison against the ground truth Shepp-Logan phantom, as shown in Figure 9. Reconstructions were completed for the entire volume, with data extracted for each central slice, as shown in Figure 10.

$$V_{norm} = \frac{v - \min}{\max - \min} \quad \text{..... (5)}$$

For Experiments 1-4 (full-scan experiments) the root mean squared error (RMSE) shown in Equation (5) (see Table 2) was used as a metric to evaluate the accuracy of the reconstructed volume against the ground truth:

$$\text{RMSE} = \sqrt{\frac{1}{n}\sum_{i=1}^{n}\left(Y_i - \hat{Y}_i\right)^2} \quad \text{..... (6)}$$

Table 2. Root mean squared error of experimental configurations

Experiment	RMSE
1	0.148
2	0.115
3	0.103
4	0.096
5	0.242
6	0.224

The structural similarity index measure (SSIM) is a metric for the perceived quality of an image that was proposed by Wang *et al*[21] as an extension of other full-reference algorithms, such as the mean squared error (MSE). The SSIM provides a quantifiable metric for the similarity of two images when viewed by a human operator. After a CT reconstruction has been performed, a human operator views the images to sentence the component. To quantify the difference between the reconstructions from the experiments performed, the SSIM, as presented in Equation (6), was applied to the 3D volume using a 3D multi-scale variation of SSIM (MS-SSIM)[22]:

$$\text{SSIM} = \frac{\left(2\mu_X\mu_Y + C_1\right)\left(2\sigma_{XY} + C_2\right)}{\left(\mu_X + \mu_Y + C_1\right)\left(\sigma_X^2 + \sigma_Y^2 + C_2\right)} \quad \text{.... (7)}$$

where μ and σ represent the average and the standard deviation of the original image X and

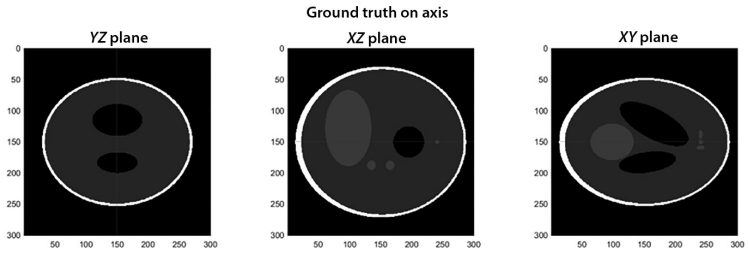

Figure 9. On-axis planes of the Shepp-Logan phantom

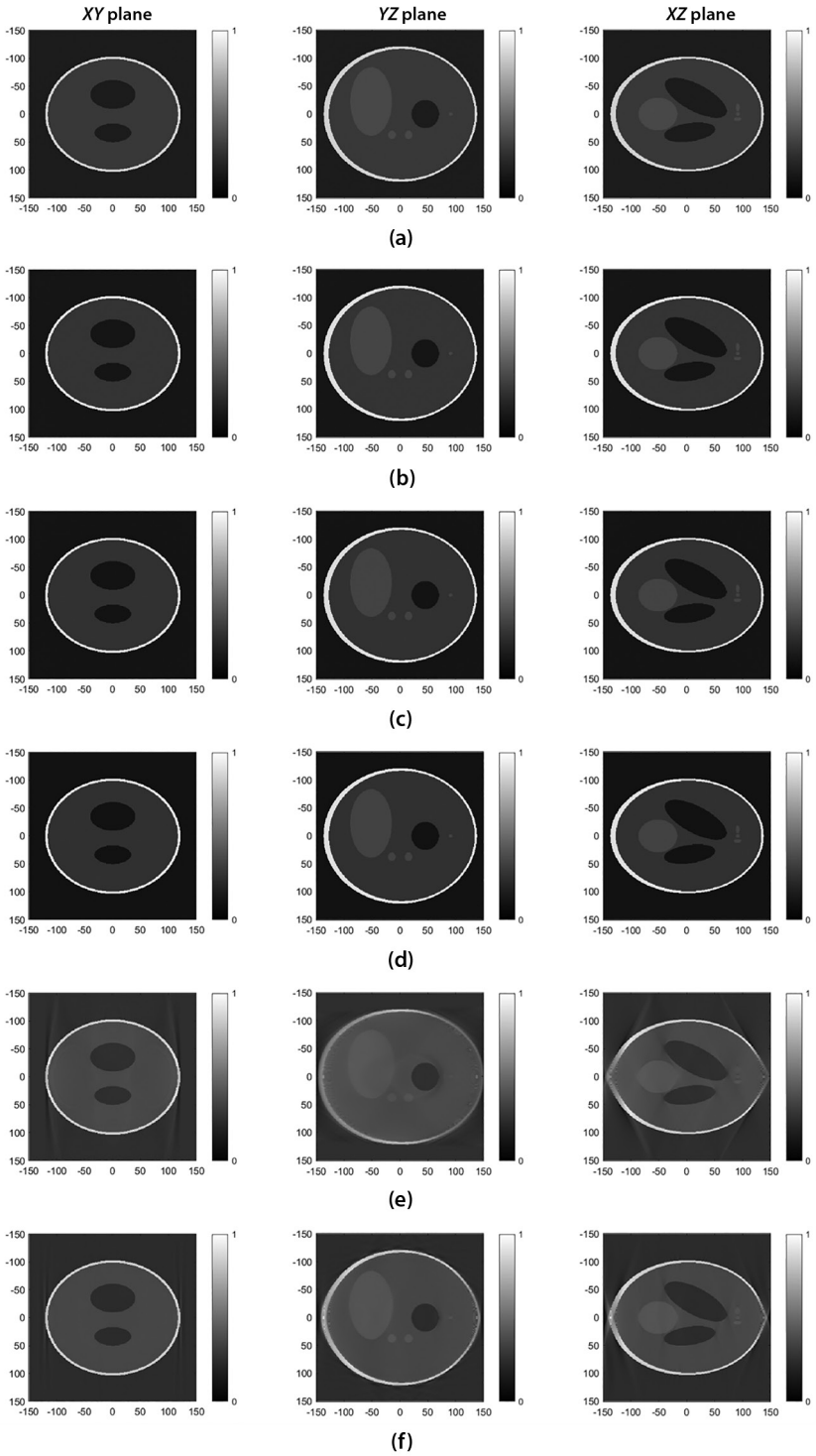

Figure 10. Reconstruction for: (a) Experiment 1; (b) Experiment 2; (c) Experiment 3; (d) Experiment 4; (e) Experiment 5; and (f) Experiment 6

the test image Y. σ_{XY} is the covariance of X and Y and the variables C_1 and C_2 are constants to ensure numerical stability. The metric was calculated using the multissim3 function in the MATLAB Image Processing Toolbox[23] and the results are presented in Table 3, where a value of 1 is an exact match.

An analysis of the 300 × 300 × 300 reconstructed volumes for all configurations was compared to the ground truth Shepp-Logan phantom to characterise the differences in error using the RMSE as a metric (shown in Table 2). The experiment with the highest error was Experiment 1, which used the circular trajectory, while Experiments 2, 3 and 4, which used a full-scan spherical trajectory, yielded a lower error. The error difference was measured as between 22% and 35% improvement. Experiment 5 demonstrated a limited-angle circular scan, which gave an RMSE of 0.242. A direct comparison between Experiments 5 and 6 (limited access spherical scan) gave an improvement of 7.5%. This demonstrated that in all of the experiments conducted, improvements were observed in the use of a spherical trajectory over that of a circular trajectory. The accuracy improvement with the spherical reconstruction technique clearly demonstrates that the use of non-circular scanning modalities is a valid strategy that can be utilised for applications such as limited-access or limited-angle acquisition.

Table 3. MS-SSIM for the six experimental configurations

Experiment	MS-SSIM
1	0.935
2	0.949
3	0.951
4	0.954
5	0.839
6	0.889

To quantify the quality of the reconstruction from the perspective of a CT operator, the SSIM was used for all six experimental configurations, with an SSIM of 1.0 being an exact match. Considering the circular trajectory, Experiment 1 gave an SSIM of 0.935, while Experiments 2, 3 and 4 gave values in a range of 0.949 to 0.954, demonstrating that reconstructed data using the spherical method performed closer to the ground truth than the corresponding circular trajectory. Similar observations can be seen for the limited-angle experimental configurations, where Experiment 5 (circular) gave a result of 0.839, compared to a value of 0.889 for the spherical. This gave an improvement in the use of the spherical trajectory over circular, albeit with a reduction over a full angular scan coverage. This is in agreement with the literature and is a consequence of not meeting the Tuy sampling criteria[24] for the circular trajectory, with the spherical providing more data for the reconstruction. However, there are many practical cases where limited-angle acquisition would be a necessary requirement due to constraints imposed by the physical size or geometry of the component. In this scenario, the methods developed in this paper would provide an advantage over the limited-angle circular scanning traditionally utilised.

Figure 11 illustrates visually the differences between the use of different trajectories for the limited-angle use-case as measured using the SSIM. Here, it can clearly be seen that the spherical method is more consistent with the size and geometry of the ground truth. The extra degrees of freedom available for this technique clearly demonstrate the ability to exploit reconstruction from source and detector positions out of the y-axis midplane.

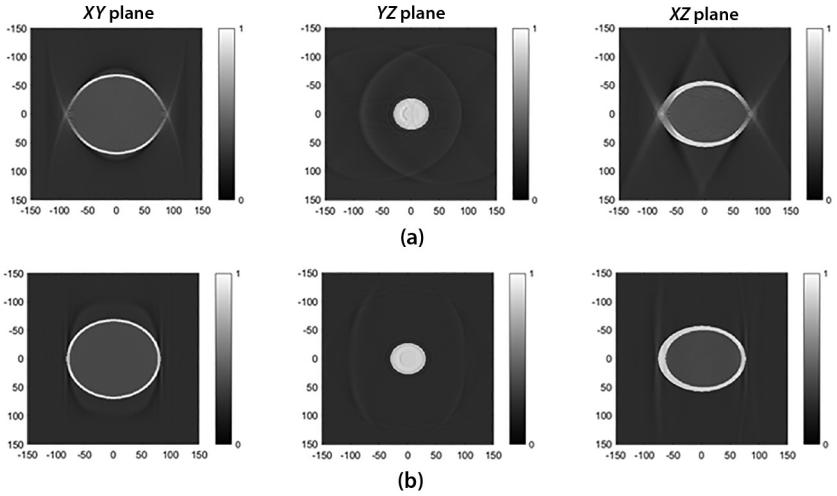

Figure 11. Reconstruction for: (a) circular limited angle; and (b) spherical limited angle

6. Conclusions

In this paper, an efficient method has been presented to reconstruct X-ray computed tomography data from non-circular acquisition trajectories using simulated data. Reconstructions were performed using the algebraic reconstruction technique and were validated against the ground truth Shepp-Logan phantom and reconstructions with the traditional circular scanning modality. The results show an increase in reconstruction accuracy compared to the circular trajectory. Non-circular trajectories were implemented to assess their suitability for reconstruction of the Shepp-Logan phantom.

The non-circular trajectory reconstructions were compared to circular trajectories that are used in traditional CT cabinet systems using standard measures, allowing an analysis of the reconstruction accuracy. The trajectories implemented had a comparable total number of projections to the circular case, with the source and detector positions distributed on the surface of a sphere instead of around a single rotation axis. The experiments performed show that the spherical trajectories have a lower reconstruction error for on-axis reconstruction planes and an overall reduction in the root mean squared error calculated for the entire volume. A non-circular limited-angle trajectory was investigated for comparison against a spherical scanning strategy, demonstrating a lower impact of artefacts traditionally associated with the use of a limited angular range. This is of great benefit to NDT when considering robotic acquisition or where access may be limited in traditional cabinet systems. Further work would seek to implement a robotic environment to assess the impact of image unsharpness, noise and other common artefacts on the reconstruction with physical acquisition and to extend the work to arbitrary robotic paths.

References

1. L A Feldkamp, L C Davis and J W Kress, 'Practical cone-beam algorithm', Journal of the Optical Society of America, Vol 1, No 6, pp 612-619, 1984.

2. C Shaw, Cone Beam Computed Tomography, CRC Press, 2014.
3. R Gordon, R Bender and G T Herman, 'Algebraic reconstruction techniques (ART) for three-dimensional electron microscopy and X-ray photography', Journal of Theoretical Biology, Vol 29, No 3, pp 471-476, 1970. DOI: 10.1016/0022-5193(70)90109-8
4. M Harakal, 'Compute unified device architecture (CUDA) GPU programming model and possible integration to the parallel environment', Proceedings of CSE 2008, Stará Lesná, Slovakia, 24-26 September 2008.
5. M Sutcliffe, M Weston, B Dutton, P Charlton and K Donne, 'Real-time full-matrix capture for ultrasonic non-destructive testing with acceleration of post-processing through graphic hardware', NDT&E International, Vol 51, pp 16-23, 2012. DOI: 10.1016/j.ndteint.2012.06.005
6. G Liaptsis, A L Clarke and P Nithiarasu, 'High-resolution X-ray volumetric inspection of large planar samples using SART-based computed laminography', Proceedings of the 56th Annual British Conference on Non-Destructive Testing (NDT 2017), Telford, UK, 5-7 September 2017.
7. A Kak and A Andersen, 'Simultaneous algebraic reconstruction technique (SART): a superior implementation of the ART algorithm', Ultrasonic Imaging, Vol 6, No 1, pp 81-94, 1984. DOI: 10.1016/0161-7346(84)90008-7
8. H K Tuy, 'An inversion formula for cone-beam reconstruction', SIAM Journal on Applied Mathematics, Vol 43, No 3, pp 546-552, 1983.
9. B D Smith, 'Cone-beam convolution formula', Computers in Biology and Medicine, Vol 13, No 2, pp 81-87, 1983. DOI: 10.1016/S0010-4825(83)80001-8
10. J R Mitchell, P Dickof and A G Law, 'A comparison of line integral algorithms', Computers in Physics, Vol 4, No 2, pp 166-172, 1990. DOI: 10.1063/1.168381
11. K Agoston, Computer Graphics and Geometric Modelling, pp 38-43, Springer, 2005.
12. J Amanatides and A Woo, 'A fast voxel traversal algorithm for ray tracing', Proceedings of the European Computer Graphics Conference and Exhibition (Eurographics '87), Amsterdam, The Netherlands, pp 3-10, 24-28 August 1987. DOI: 10.1.1.42.3443
13. T L Kay and J T Kajiya, 'Ray tracing complex scenes', Proceedings of the 13th Annual Conference on Computer Graphics and Interactive Techniques (SIGGRAPH 1986), Vol 20, No 4, pp 269-278, 1986. DOI: 10.1145/15922.15916
14. P Landstorfer, G Herl and J Hiller, 'Investigation of non-circular scanning trajectories in robot-based industrial X-ray computed tomography of multi-material objects', Proceedings of the 16th International Conference on Informatics in Control, Automation and Robotics (ICINCO 2019), Vol 2, pp 518-522, 2019. DOI: 10.5220/0007966405180522
15. P Chen, Y Han and Z Gui, 'CT scanning imaging method based on a spherical trajectory', PLOS One, Vol 11, No 3, pp 1-13, 2016. DOI: 10.1371/journal.pone.0149779
16. L A Shepp, B F Logan and M Hill, 'The Fourier reconstruction of a head section', IEEE Transactions on Nuclear Science, Vol 21, No 3, pp 21-43, June 1974.
17. A V Narasimhadhan and K Rajgopal, 'FDK-type algorithms with no back-projection weight for circular and helical scan CT', International Journal of Biomedical Imaging, Vol 2012, 969432, 2012. DOI: 10.1155/2012/969432
18. G Wang, Y Liu, T H Lin and P C Cheng, 'Half-scan cone-beam X-ray microtomography formula', Scanning, Vol 16, No 4, pp 216-220, 1994. DOI: 10.1002/sca.4950160406
19. R Clackdoyle and M Defrise, 'Region-of-interest reconstruction from incomplete data', IEEE Signal Processing Magazine, pp 60-80, 2010.
20. S Gondrom, J Zhou, M Maisl, H Reiter, M Kröning and W Arnold, 'X-ray computed laminography: an approach of computed tomography for applications with limited access', Nuclear Engineering and Design, Vol 190, No 1-2, pp 141-147, 1999. DOI: 10.1016/S0029-5493(98)00319-7
21. Z Wang, A C Bovik, H R Sheikh and E P Simoncelli, 'Image quality assessment: from error visibility to structural similarity', IEEE Transactions on Image Processing, Vol 13, No 4, pp 600-612, 2004. DOI: 10.1109/TIP.2003.819861
22. J Søgaard, L Krasula, M Shahid, D Temel, K Brunnström and M Razaak, 'Applicability of existing objective metrics of perceptual quality for adaptive video streaming', IS&T International Symposium on Electronic Imaging Science and Technology, 2016. DOI: 10.2352/ISSN.2470-1173.2016.13.IQSP-206
23. MathWorks United Kingdom, 'Multiscale structural similarity (MS-SSIM) index for volume quality – MATLAB multissim3'. Available at: https://uk.mathworks.com/help/images/ref/multissim3.html (Accessed: 12 December 2021).
24. Z Zhang and L J Bond, 'A review of reconstruction methods for limited-angle X-ray tomography in non-destructive evaluation applications', Review of Progress in Quantitative Nondestructive Evaluation, 2019.

©2022 TWI Ltd